López del Moral, D.; Barrado, A.; Sanz, M.; Lázaro, A.; Fernández, C.; Zumel, P. Analysis and implementation of the Autotransformer Forward-Flyback converter applied to photovoltaic systems . In: *Solar energy, vol. 194, Dec. 2019, Pp. 995-1012.*

DOI: https://doi.org/10.1016/j.solener.2019.10.082

Analysis and implementation of the Autotransformer Forward-Flyback converter applied to photovoltaic systems

D. López del Moral, A. Barrado, M. Sanz, A. Lázaro, C. Fernández, P. Zumel
Universidad Carlos III de Madrid
Electronic Technology Department
Power Electronics Systems Group
Avda. Universidad, 30; 28911, Leganés, Madrid, SPAIN
E-mail: dmoral@ing.uc3m; andres.barrado@uc3m.es

Abstract:

The Distributed Maximum Power Point Tracking (DMPPT) architecture is employed to overcome the mismatching phenomena in grid-tied photovoltaic (PV) installations. In this kind of architecture, a DC-DC module integrated converter (MIC) manages each PV panel. Thanks to the DC-DC converters, the differences between PV panels do not influence others, maximising the amount of harvested power. The MIC requirements to make this kind of solutions profitable are high efficiency, low cost and the capability of voltage step-up and step-down. This paper analyses the Autotransformer Forward-Flyback (AFF) converter. This converter is considered as a MIC candidate for fulfilling the requirements above. The study of the AFF converter includes the steady-state analysis and the small signal analysis in continuous conduction mode. The AFF converter advantages are its step-up and step-down voltage transfer function; a higher simplicity since it only includes a single controlled switch; the soft switching characteristics in all the diodes; the use of an autotransformer; and good dynamic performances. A step-by-step design procedure focused on a100 kW grid-tied PV installation, with some PV panels affected by shadows, is explained. The theoretical analyses are validated through the experimental results in a 225 W AFF prototype, achieving an efficiency up to 94.5 %.

Keywords: DC/DC converter, photovoltaic, efficiency, DMPPT, module integrated converters, autotransformer

1. Introduction

Photovoltaic energy is one of the most relevant energy sources. As shown in Figure 1, the PV Cell/Module production is almost exponentially increasing from 2010 to 2018 [1]. This fact, along with the social awareness makes this field worthy and motivates research in the improvement of current PV conversion technologies and the development of new ones.

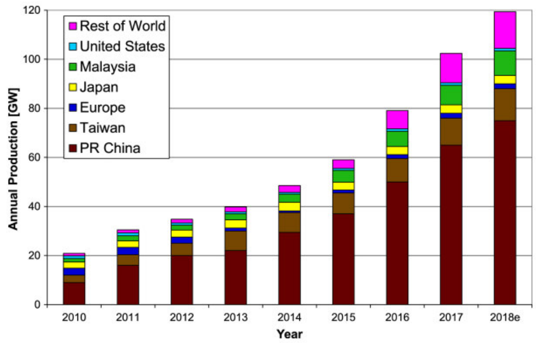

Figure 1. World PV Cell/Module Production from 2010 to 2018 [1]

Many PV panels are required to generate a high amount of power in PV grid-tied installations. To improve the inverter efficiency, it is a good practice to keep constant the inverter's input voltage. Several PV panels are connected in series in the same string to achieve the desired inverter input voltage. It is well known that PV panels connected to the same string share the same output current.

Therefore, a variation in the electrical characteristic of one of the PV panels connected to the string implies a variation in the rest of the string-connected PV panels, reducing the generated power drastically, even when the irradiation conditions are optimum.

The difference in the PV panels characteristics or the environmental conditions is known as the mismatching phenomena. This issue is considered as one of the most critical issues in PV installations. The mismatching is commonly caused by temperature differences, dirt, shadows, aging, etc., [2] - [3]. The mismatching effect in the PV panel electrical characteristics is deeply studied in the literature [4] - [7].

To overcome the mismatching issue, one of the most standard solutions is the isolation of each PV panel from the rest of the PV panels in the PV installation. A DC-DC Module Integrated Converter (MIC) can be used to achieve the isolation and the maximum harvested power. This kind of PV architecture is known as Distributed Maximum Power Point Tracking (DMPPT) architecture [8] - [14], see Figure 2. The main drawback of DMPPT architectures is the high number of MIC required, that increase the cost of the installation.

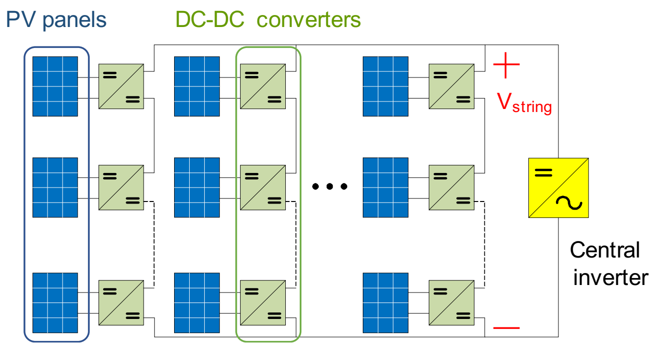

Figure 2. PV grid-tied installation with the DMPPT architecture

To make the PV installation profitable, the MIC should have high efficiency, low cost and the capability of voltage step-up and step-down. Several references are focused on the efficiency converters improvement, to fulfil these desired requirements. One of the strategies explored to improve the efficiency of the converter is not to process the full amount of power delivered to the load. This kind of topologies are known as Partial-Power Conversion (PPC), Series Connection, Parallel-Power-Processed (PPP) or Direct Energy Transfer (DET) converters [15] – [23]. In all of them, the efficiency improvement is achieved due to the converter only manages a part of the energy, whereas the rest of the output power is directly delivered to the load. The best efficiency achieved in these converters is up to 98 % in [16]. The main constraint of this kind of topologies is that it can only be used to voltage step-up, reducing the string-configuration possibilities in the PV installation. Beyond the topologies, that does not process the full power, other authors have also obtained efficiencies around 98 % with full power processing topologies, but these topologies are not capable of both voltage step-down and step-up [24] - [26].

The MIC cost is a variable difficult to estimate because it depends on the manufacturing volumes, and hardly ever is analyzed in the literature. As a rough parameter, the number of components employed in the converters could be used to estimate the cost of the converter, although not all the components cost the same. In any case, this parameter is going to be used in this paper.

Although any DC-DC converter can be employed in PV installations, several authors have demonstrated that the highest flexibility regarding the number of PV panels per string is only achieved with voltage step-up and step-down converters [27] - [30]. Within the voltage step-up and step-down topologies, one of the most promising ones is the classical Non-Inverting Buck-Boost converter [27] and [31]. Although very high efficiencies have been obtained in [27], some drawbacks of this topology are the high current through the inductor and switches, and the needed of four switches and drivers. Therefore, the complexity and the components count increases.

On the other hand, although the achieved efficiency is not as high as the one obtained in [27], in [32] is introduced a topology that fulfils all the desired MIC requirements for being applied to grid-tied PV installations with DMPPT architectures, the Buck-Boost Modified Forward Series (BBMSF) converter.

The topology analysed in this paper is the Autotransformer Forward-Flyback (AFF) converter. This topology can be considered as an evolution of the BBMSF converter, and therefore, it can be considered as a good MIC candidate to be applied in DMPPT architectures. Some advantages of the AFF converter are the voltage step-up and step-down capability, its high efficiency and its simplicity due to it only has one switch, so it only requires one driver. Also, thanks to the autotransformer connection, only a part of the output power is magnetically processed, reducing the autotransformer power losses and reactive energy of the converter.

The paper is organized as follows: in Section 2, a complete analysis of the AFF converter is carried out, including the time domain analysis as well as the frequency domain analysis in continuous conduction mode. In Section 3, the experimental results, obtained with a 225 W AFF prototype, verify the theoretical analysis. The conclusions of the paper are detailed in Section 4.

2. THEORETICAL ANALYSIS OF THE AFF CONVERTER

An in-depth analysis of the Autotransformer Forward-Flyback (AFF) converter, which has already been introduced in [33], is carried out in the present paper. The AFF topology is an evolution of the Buck-Boost Modified Series Forward (BBMSF) converter [32]. In Figure 3 it is highlighted the main difference between both topologies which is related to the autotransformer reset.

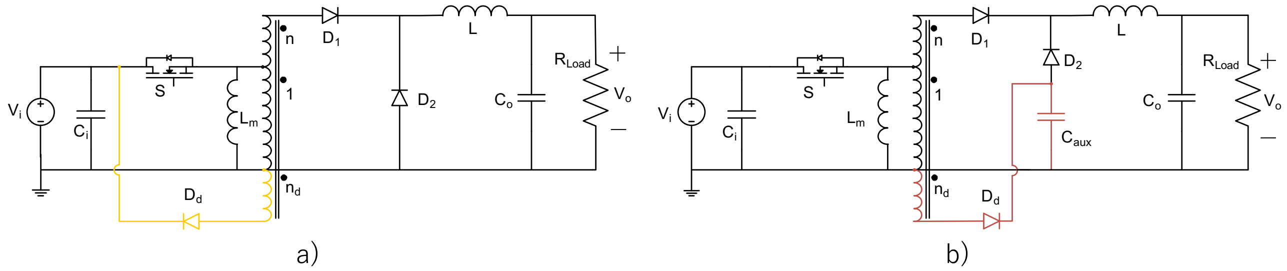

Figure 3. Comparison between the BBMSF converter topology (a)) and the AFF converter topology (b))

In the BBMSF converter, the autotransformer delivers its previously stored magnetising energy into the input capacitor, however, in the AFF converter, it is delivered to an auxiliary capacitor, C_{aux}. This different autotransformer reset network connection has important consequences in the converter behaviour and performances. Indeed, due to this connection, the AFF topology can be considered as a combination between the Forward converter and the Flyback converter, see Figure 4.

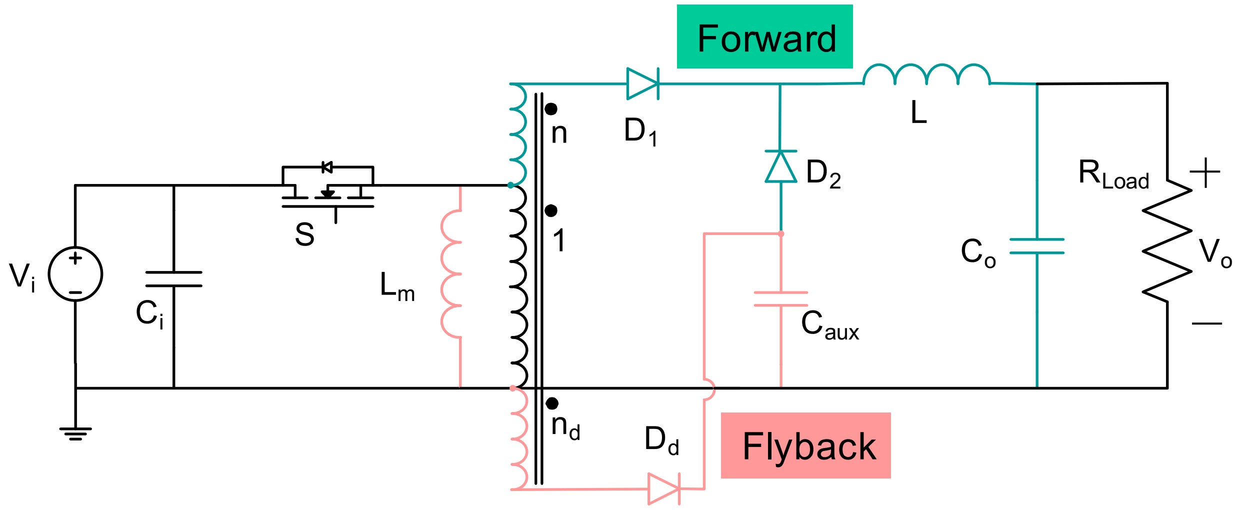

Figure 4. AFF converter as a Forward and a Flyback converter combination

Figure 4 shows how the Forward-net output and the Flyback-net output delivers energy to the load. This fact can also be appreciated in the output-input voltage transfer function obtained in Section 2.2. Besides, thanks to the voltage fixed into the C_{aux} capacitor, the D_2 diode blocks a low voltage. Therefore, a high-performance diode is selected, improving the converter efficiency, as shown in Section 3.1.2.

2.1 PRINCIPLE OF OPERATION

The AFF converter can be operated in several modes, depending on the conduction mode of each one of their inductors, L and L_m. Theoretically, the converter offers four possibilities, as summarised in Table I.

Table I. AFF converter operational modes

Operational Mode	L conduction mode	L_m conduction mode
OM1	CCM	CCM
OM2	CCM	DCM
OM3	DCM	CCM
OM4	DCM	DCM

In the operational modes with inductors working in DCM, OM2 to OM4, the RMS currents through the magnetic devices are higher than in CCM, for the same output power. Higher RMS currents tend to imply higher DC losses and higher size magnetic devices. Therefore, all the analyses carried out in this paper refers to the OM1, where both magnetic inductances L and L_m work in CCM.

Regarding the principle of operation, two main intervals can be defined depending on the MOSFET state: $t_{ON,}$ while the S MOSFET is switched on; and t_{OFF}, while it is switched off.

Figure 5 to Figure 6 depict the current paths followed by the current in each interval.

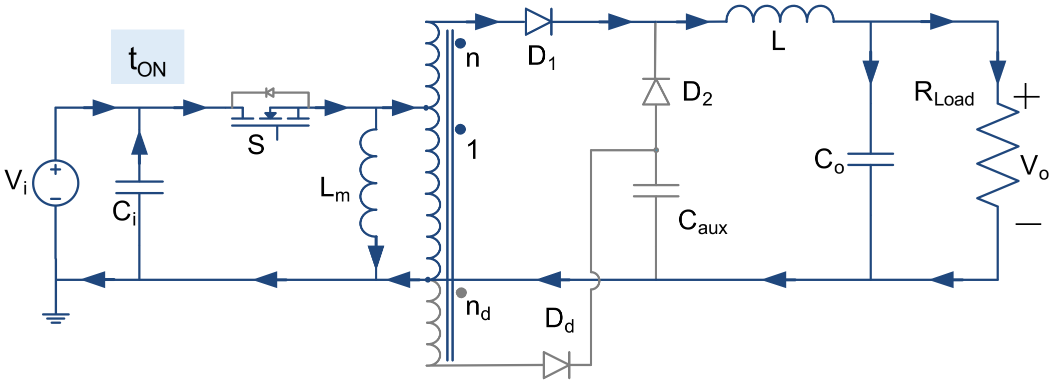

Figure 5. AFF current paths during the t_{ON} interval

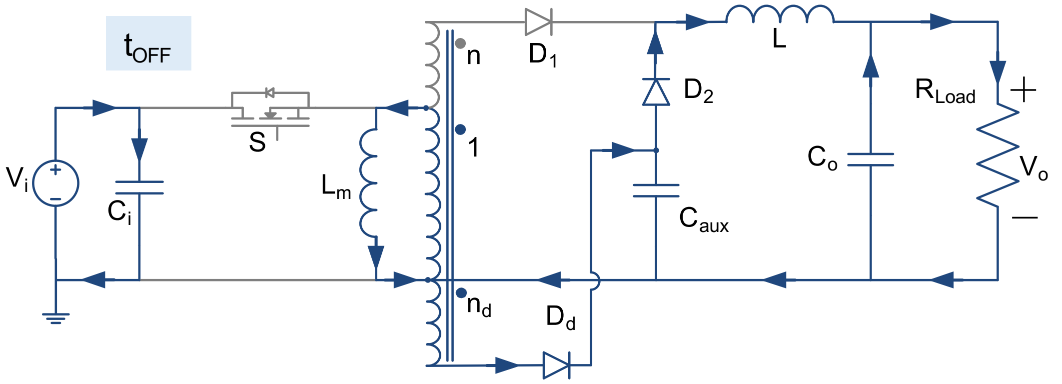

Figure 6. AFF current paths during the t_{OFF} interval

As it can be seen, the current paths are highlighted in blue colour, whereas the rest of the circuit is depicted in grey colour. The direction of the current is denoted with arrows. For the sake of simplicity, the model described in this analysis is ideal, without taking into account the parasitic inductances, capacitances and resistances that are in real converters.

- t_{ON}

As it has been mentioned before, the first interval corresponds to the time while the S MOSFET is switched on. During this interval, both inductances, L and L_m, are storing energy.

The converter delivers the power from the input to the output filter through the S MOSFET, the autotransformer and the D_1 diode, see Figure 5. Thanks to the autotransformer connection, only a part of the output power is magnetically processed, increasing the converter's efficiency.

- t_{OFF}

Once the MOSFET is switched off, the reset of both the output inductance L and the magnetising inductance L_m begins. As it can be seen in Figure 6, the previously stored energy in L_m is delivered to the C_{aux} capacitor and the output filter, through the diodes D_d and D_2. The L current also flows through the D_d and D_2. Analyzing this operation could seem that both "current sources" are connected in series, but the C_{aux} capacitor decouples one from the other. A detail of the currents distribution at this junction point is shown in Figure 7.

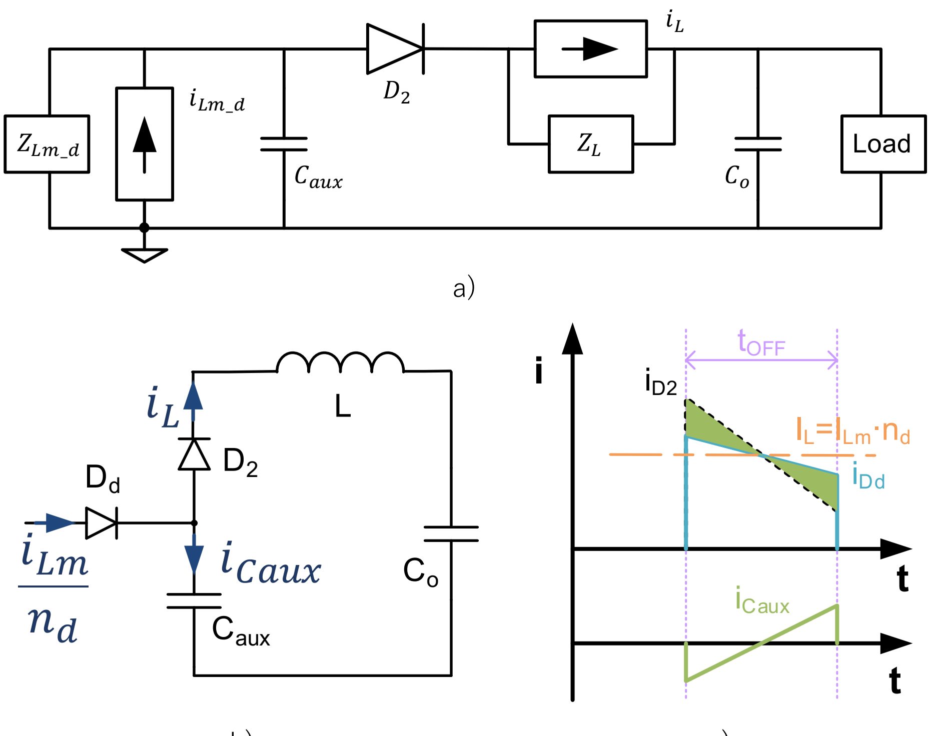

Figure 7. Current distribution detail in the Dd, D2 and Caux junction point during the t_{OFF} interval of the AFF converter. a) Equivalent current sources model b) Electrical scheme; c) Current waveforms

In Figure 7a), the suffix "_d" denotes that the variables are referred to the tertiary winding (n_d), meaning:

$$Z_{Lm\_d} = Z_{Lm} \cdot n_d^2 \qquad (1)$$

$$i_{Lm\_d} = \frac{i_{Lm}}{n_d} \qquad (2)$$

It is noteworthy that, during this switching interval, Figure 7c), the average value of the output inductor current is the same as the magnetising inductance current referred to the tertiary winding of the autotransformer, see (3). The difference between both currents is compensated by the C_{aux} capacitor.

$$I_{Lm} = I_L \cdot n_d \qquad (3)$$

This interval ends when the S MOSFET switches on again, starting a new cycle.

In Table II are summarised the main events of each switching interval.

Table II. Summary of the principle of operation events for the AFF converter

Switching interval	Start event	Main considerations	Final event
t_{ON}	S is turned on	L and L_m → store energy Part of the output power → magnetically processed D_1 → positive biased	S is turned off
t_{OFF}	S is turned off	L and L_m → deliver energy Caux → decouples i_L and i_{Lm} D_2 and D_d → positive biased	S is turned on

2.2 STATE-STAGE AND TIME DOMAIN ANALYSIS IN CONTINUOUS CONDUCTION MODE

The expression that defines a DC-DC converter used as a voltage source is the output-input voltage transfer function. A voltage-per-second balance in the output filter inductor L is carried out to obtain this expression. In (4), the AFF converter output-input voltage transfer function in OM1, see Table I, is calculated.

$$\frac{V_o}{V_i} = (1 + n + n_d) \cdot D \tag{4}$$

As it can be seen, the output-input voltage transfer function includes a contribution of both n and n_d variables, Forward-net and Flyback-net, see Figure 4.

The AFF converter presents a duty cycle limitation, see (5). The restriction comes from the fact that the Flyback-net output voltage must be lower than the Forward-net one. Otherwise, the D_1 diode is never directly biased.

$$d \leq \frac{1 + n}{1 + n + n_d} \tag{5}$$

Next, the current and voltage stresses are analyzed for each one of the AFF converter components. The variables denoted with capital letters indicates average or steady-state values, whereas the variables denoted with lower case letters indicate time dependence.

- Output filter inductance (L)

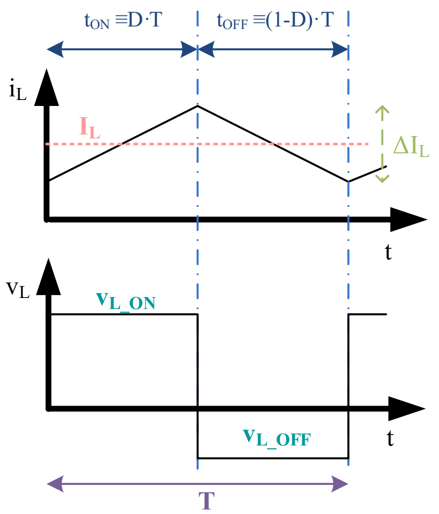

Figure 8. Output inductor current and voltage waveforms, i_L and v_L respectively, during a switching period.

$$\Delta I_L = \frac{V_i \cdot D \cdot [(1 + n) \cdot (1 - D) - n_d \cdot D]}{L \cdot f_{sw}} \tag{6}$$

$$I_L = I_{string} = \frac{P}{V_i \cdot (1 + n + n_d) \cdot D} \tag{7}$$

$$v_{L\_ON} = v_i \cdot [(1 + n) - d \cdot (1 + n + n_d)] \tag{8}$$

$$v_{L\_OFF} = -v_i \cdot [(1 + n) - d \cdot (1 + n + n_d)] \cdot \frac{d}{1 - d} \tag{9}$$

- Autotransformer

The design of the autotransformer is crucial. As it can be seen in (4), the output voltage is highly dependent on the autotransformer turn ratios n and n_d. Rearranging the equation (5) obtains the maximum tertiary turn ratio n_d for a desired maximum duty cycle and a fixed primary turn ratio n (10).

$$n_d \leq \frac{(1+n)\cdot(1-d)}{d} \tag{10}$$

Several currents can be used to define the autotransformer behaviour. However, only the magnetising voltage and current are obtained in this section. The rest of the autotransformer currents can be obtained from other components: the primary current is the same as the S MOSFET current, the secondary current is the same as the D_1 diode current, and the tertiary current corresponds with the D_d diode.

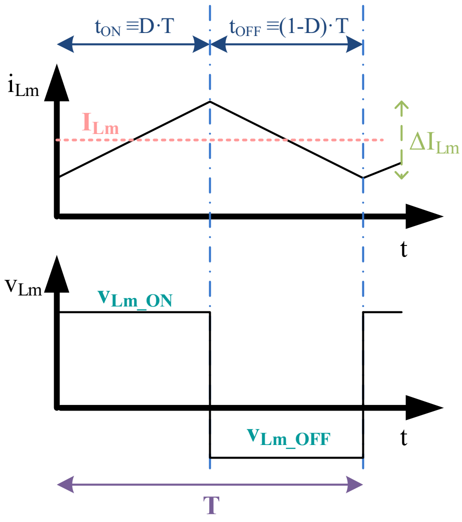

Figure 9. Magnetizing inductor current and voltage waveforms, i_{Lm} and v_{Lm} respectively, during a switching period.

$$\Delta I_{Lm} = \frac{V_i \cdot D}{L_m \cdot f_{sw}} \tag{11}$$

$$I_{Lm} = I_L \cdot n_d \tag{12}$$

$$v_{Lm\_ON} = v_i \tag{13}$$

$$v_{Lm\_OFF} = -v_i \cdot \frac{d}{1-d} \tag{14}$$

- MOSFET (S)

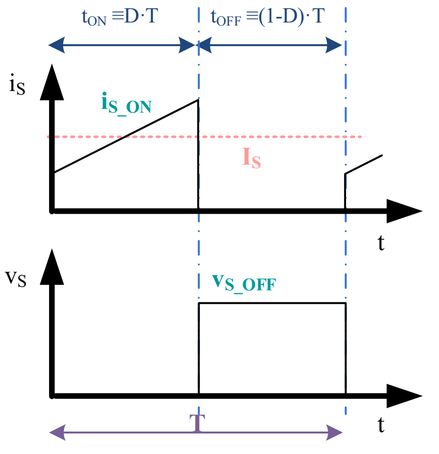

Figure 10. MOSFET current and voltage waveforms, i_{DS} and v_{DS} respectively, during a switching period.

$$i_{S\_ON} = i_L \cdot (1+n) + i_{Lm} \tag{15}$$

$$I_S = I_L \cdot (1+n+n_d) \cdot D \tag{16}$$

$$v_{S\_OFF} = v_i \cdot \frac{1}{1-d} \tag{17}$$

- D_1 diode

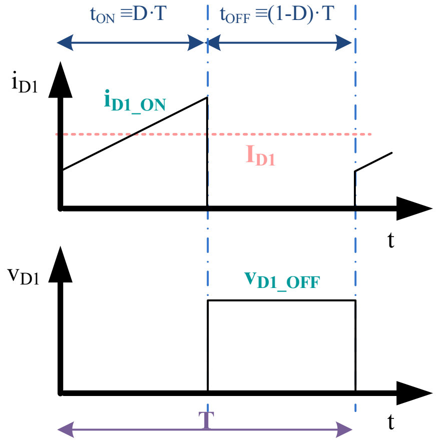

Figure 11. D_1 diode current and voltage waveforms, i_{D1} and v_{D1} respectively, during a switching period.

$$i_{D1\_ON} = i_L \tag{18}$$

$$I_{D1} = I_L \cdot D \tag{19}$$

$$v_{D1\_OFF} = v_i \cdot \frac{(1 + n + n_d) \cdot d}{1 - d} \tag{20}$$

- D_2 diode

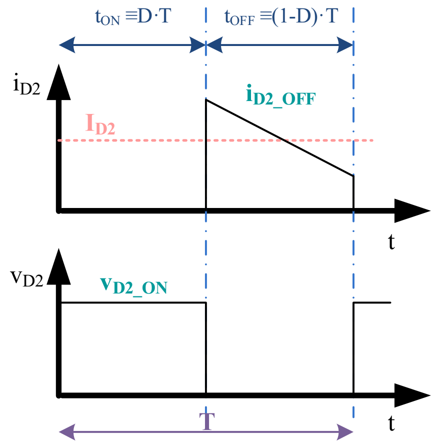

Figure 12. D_2 diode current and voltage waveforms, i_{D2} and v_{D2} respectively, during a switching period.

$$i_{D2\_OFF} = i_L \tag{21}$$

$$I_{D2} = I_L \cdot (1 - D) \tag{22}$$

$$v_{D2\_ON} = v_i \cdot \frac{(1 + n) - d \cdot (1 + n + n_d)}{1 - d} \tag{23}$$

- D_d diode

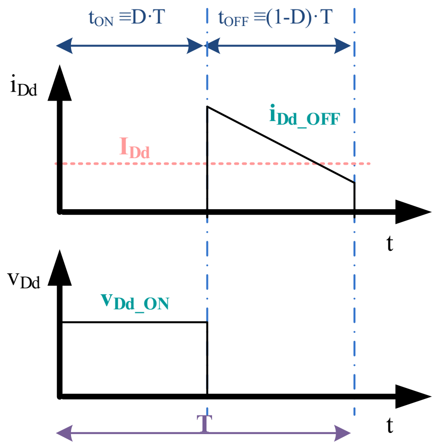

Figure 13. D_d diode current and voltage waveforms, i_{Dd} and v_{Dd} respectively, during a switching period.

$$i_{Dd\_OFF} = \frac{i_{Lm}}{n_d} \tag{24}$$

$$I_{Dd} = I_L \cdot (1 - D) \tag{25}$$

$$v_{Dd\_ON} = v_i \cdot \frac{n_d}{1 - d} \tag{26}$$

A. Power transfer analysis

The connection of the autotransformer is one of the critical points of the AFF converter. Thanks to this connection, only a part of the delivered power is magnetically processed by the autotransformer. The size of the autotransformer and its power losses are therefore reduced.

In this section, the theoretical expression that defines the power percentage managed by the autotransformer in OM1 is calculated.

Using the equation (4) in the output power expression, (27) is obtained.

$$P_o = V_o \cdot I_o = (1 + n + n_d) \cdot D \cdot V_i \cdot I_o = D \cdot V_i \cdot I_o + (n + n_d) \cdot D \cdot V_i \cdot I_o = P_{not\_mag} + P_{mag} \tag{27}$$

From the equation (27), the relation between the magnetically processed and not magnetically processed power transference, P_{mag} and P_{not_mag} respectively, is calculated:

$$\frac{P_{mag}}{P_{not\_mag}} = n + n_d \tag{28}$$

The percentages of both P_{not_mag} and P_{mag} with respect the output power are described in equations (29) and (30) respectively.

$$P_{not\_mag} = \frac{1}{1 + n + n_d} \cdot P_o \tag{29}$$

$$P_{mag} = \frac{n + n_d}{1 + n + n_d} \cdot P_o \tag{30}$$

In Table III, several cases regarding turns ratio parameter are selected to illustrate the equations (29) and (30).

Table III. Magnetically and not magnetically processed power percentage

$n+n_d$	0.1	0.5	1	1.5	2
P_{not_mag} (%)	0.909	0.667	0.500	0.400	0.333
P_{mag} (%)	0.091	0.333	0.500	0.600	0.667

As it can be seen, the lower the turns ratios n and n_d, the lower P_{mag} percentage. Consequently, for a higher efficiency, low turns ratios values are desired. On the other hand, low turn ratios limit the voltage step-up, see (4).

Section 3.1.2 describes the process to select the best turn ratios values for a particular case of study.

2.3 Small-signal model. Frequency domain analysis

Classic model techniques based on averaging, linearization and perturbation have been employed to obtain the small signal model of the AFF converter in OM1 [34], see Figure 14.

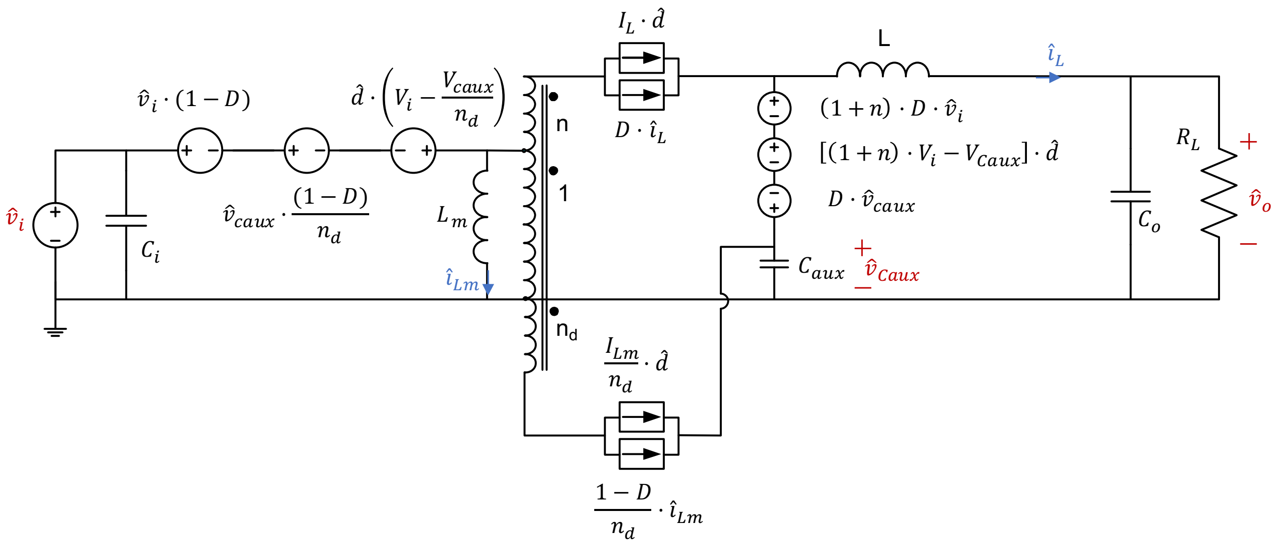

Figure 14. Small signal model of the AFF converter

In Figure 14 the capital letters refer to DC values for a specific operational point, whereas the disturbed variables are denoted with the superscript "∧".

The injected current method is employed to obtain the small signal transfer functions [34]. In this method, the main small signal transfer functions can be obtained through the current injected into the load. Figure 15 depicts the block diagram that describes the method above.

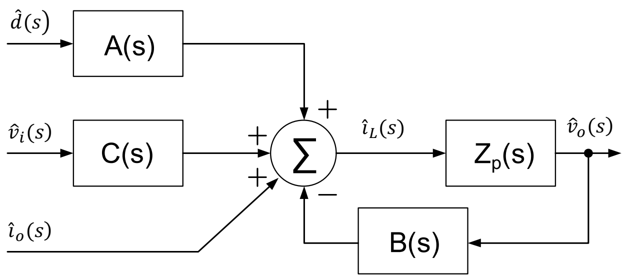

Figure 15. A small signal block diagram

Therefore, to obtain the small signal transfer functions, the expression that relates the injected current i_L in terms of the duty cycle, the input voltage and the output voltage is needed, see (31).

$$\hat{\imath}_L(s) = A(s) \cdot \hat{d} - B(s) \cdot \hat{v}_o + C(s) \cdot \hat{v}_i \tag{31}$$

Solving the circuit of Figure 14, the terms of the current through the output inductor i_L, the A(s), B(s) and C(s) terms can be obtained. The specific values for the AFF converter are summarized in Table IV.

Table IV. Expressions of the AFF converter small signal blocks

Small signal block	Expression
$A(s)$	$\dfrac{(1+n)\cdot V_i - V_{Caux} + \dfrac{(1-D)^2\cdot N(s)\cdot\left(V_i + \dfrac{V_{Caux}}{n_d}\right)}{n_d\cdot Z_{Lm}(s)}}{Z_L(s) + (1-D)^2\cdot N(s)}$
$B(s)$	$\dfrac{1}{Z_L(s) + (1-D)^2\cdot N(s)}$
$C(s)$	$\dfrac{(1+n)\cdot D + \dfrac{D\cdot(1-D)^2\cdot N(s)}{n_d\cdot Z_{Lm}(s)}}{Z_L(s) + (1-D)^2\cdot N(s)}$
$N(s)$	$\dfrac{n_d^2\cdot Z_{Lm}(s)\cdot Z_{Caux}(s)}{n_d^2\cdot Z_{Lm}(s) + Z_{Caux}(s)\cdot(1-D)^2}$
$Z_{Caux}(s)$	$\dfrac{1}{s\cdot C_{aux}}$
$Z_L(s)$	$s\cdot L$
$Z_{Lm}(s)$	$s\cdot L_m$
$Z_p(s)$	$\dfrac{R_L}{1 + s\cdot C_o\cdot R_L}$

The most common expressions used for defining the dynamic performances of a converter are the output voltage-duty cycle gain $G_{vd}(s)$, the output-input voltage gain (audiosusceptibility) $G_{vv}(s)$ and the output impedance $Z_o(s)$. These expressions can be calculated for the AFF converter, replacing in (32) - (34) the $A(s), B(s), C(s)$ and $Zp(s)$ expressions, detailed in Table IV.

$$G_{vd}(s) = \frac{\hat{v}_o}{\hat{d}} = \frac{A(s)\cdot Z_p(s)}{1 + B(s)\cdot Z_p(s)} \tag{32}$$

$$G_{vv}(s) = \frac{\hat{v}_o}{\hat{v}_i} = \frac{C(s)\cdot Z_p(s)}{1 + B(s)\cdot Z_p(s)} \tag{33}$$

$$Z_o(s) = \frac{\hat{v}_o}{\hat{\imath}_o} = \frac{Z_p(s)}{1 + B(s)\cdot Z_p(s)} \tag{34}$$

A four-order polynomic is obtained by expanding the denominator of the expressions (32) - (34). This means that there are four poles in the small signal transfer functions. The four poles are indeed two double poles. The frequency of these pole-pairs is described in (35) and (36):

$$f_{pole\_Fl} = \frac{1}{2\cdot\pi\cdot\sqrt{L_{m\_eq}\cdot C_{aux}}} \tag{35}$$

$$f_{pole\_Fw} = \frac{1}{2 \cdot \pi \cdot \sqrt{L \cdot C_o}} \tag{36}$$

where $L_{m\_eq} = \frac{L_m \cdot n_d^2}{(1-D)^2}$.

As it is denoted in the suffix of the frequency variables (35) and (36), the lowest frequency is directly dependent on the Flyback-net of the AFF converter, whereas the highest frequency depends on the Forward-net of the AFF converter, see Figure 4. For avoiding the overlapping of the poles-frequencies effects, it is recommended (37):

$$f_{pole\_Fl} < f_{zeroes} < f_{pole\_Fb} \tag{37}$$

An overlap between the poles-frequencies, without the zeroes correction, yields in a phase shift of -180 degrees, reducing the chances of obtaining high bandwidth.

Regarding the zeroes of the (32) - (34) small signal transfer functions, the output voltage-duty cycle and the audio-susceptibility have double zeroes whereas the output impedance denominator has a zero in the origin and double zeroes.

Some simulations are carried out in the next section to validate the theoretical analysis.

2.3.1 Simulation validation

Each one of the small signal transfer function expressions, obtained in the previous section in (32) - (34), is depicted in Mathcad® and compared with the simulation results obtained with PSIM®. The specific values employed for this comparison are summarized in Table V.

Table V. Parameters of the AFF converter for a non-shaded PV panel in Scenario 1

Parameter	Definition	Value
f_{sw}	Switching frequency	50 kHz
V_i	Input voltage	29.3 V
D	Duty cycle	0.689
n	Autotransformer secondary turns ratio	0.5
n_d	Autotransformer tertiary turns ratio	0.5
L	Output filter inductance	33 μH
L_m	Magnetizing inductance	185 μH
C_o	Output filter capacitance	112 μF
C_{aux}	Auxiliary capacitance	100 μF
R_L	Output load	7.255 Ω

All the values shown in Table V corresponds to the ones selected in the prototyping step, for a non-shaded PV panel in Scenario 1. The case of study and converter specifications are defined in the converters design Section 3.1.

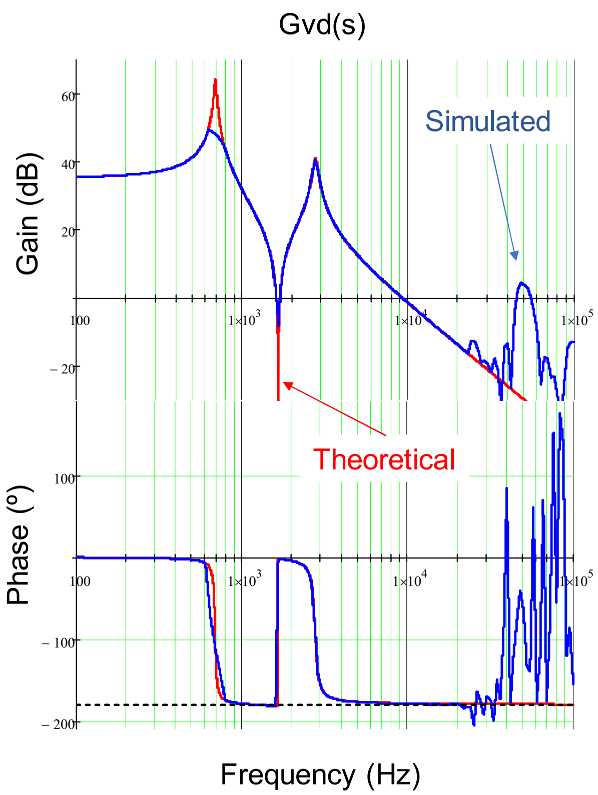

Figure 16. AFF converter output voltage-duty cycle small signal transfer function, Gvd(s)

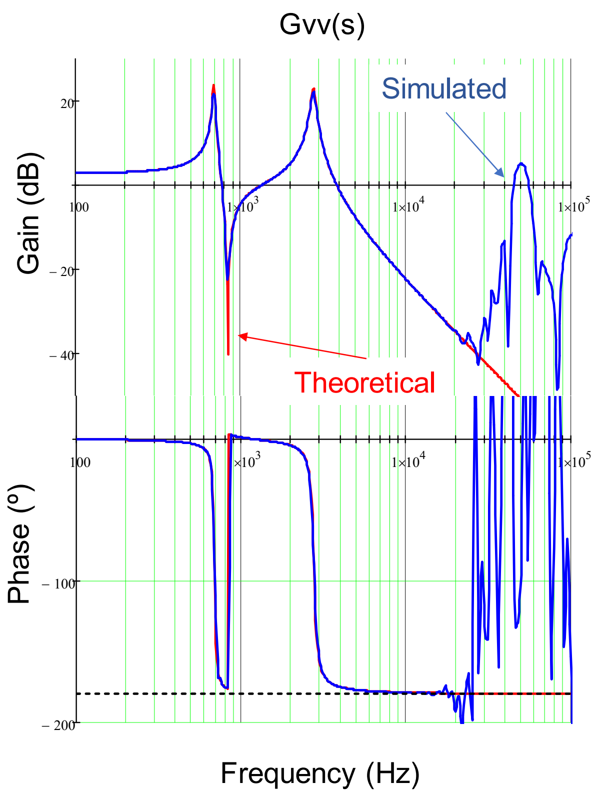

Figure 17. AFF converter audio-susceptibility, Gvv(s)

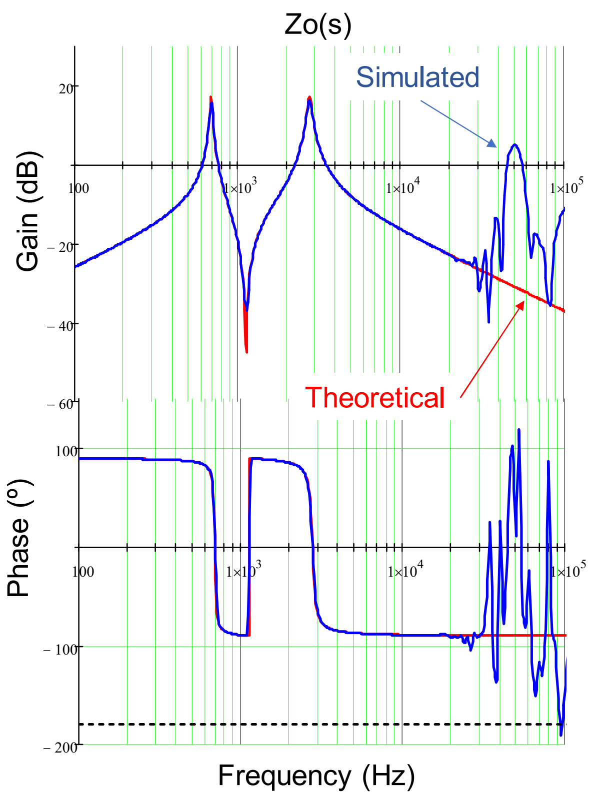

Figure 18. AFF converter output impedance, Zo(s)

Figure 16 to Figure 18 depict the small signal transfer functions corresponding to expressions (32) - (34) respectively. The theoretical representation is depicted in red colour, whereas the simulated one is depicted in blue colour. By comparing both, the theoretical and simulated graphs, it can be noted that the theoretical results fit the simulated ones up to around 20 kHz, which is almost half of the employed switching frequency. From this frequency on, the simulation results are no longer representative.

As expected, two double poles can be appreciated in the three small signal representations. The frequencies of these poles are the same in all of them. The double zeroes can also be appreciated in both, the gains and phases in Figure 16 - Figure 18. The effect of the zero in origin can be seen in the output impedance small signal transfer function.

Depending on the relation between the poles frequencies and the double zero frequency, the phase step could reach 360 degrees. This fact should be considered when designing the converter regulator.

3. EXPERIMENTAL VERIFICATION

3.1 CONVERTER DESIGN

3.1.1 The case of study/application environment

A prototype must be designed and tested to verify the previous theoretical analysis. Depending on the application, some decisions should be taken to select the proper components. The field of application, in this case, is a 100 kW grid-tied photovoltaic installation with DMPPT architecture, see Figure 2. In this kind of installations, the central inverter operating voltage is critical, due to it fixes the string voltage. The *FREESUN LVT FS0100* inverter is selected for this case of study [35]. This inverter has a 600 V input voltage. Once the central inverter is selected, several PV panels can be chosen. Depending on the type of PV panel, different maximum power point, open circuit and short circuit characteristics must be taken into account. The 225 W *SKJ60P6L* PV panel, from Siliken, is the one included in this study [36].

The desired 100kW of the PV installation requires 450 PV panels of 225 W each. The voltage step-up and step-down capability of the AFF converter allows multiple combinations of the number of strings – the number of PV panels per string. In this case, the selected DMPPT configuration is formed by 25 strings with 18 PV panels in series per string.

For taking into account the effect of mismatching, two different scenarios have been defined, depending on the percentage of shaded PV panels. In the Scenario E0, there are no shaded PV panels; whereas a 25% percentage of the PV panels are affected by shadows in the Scenario E1. As it is described in [2], a shadow in a PV panel can drastically reduce both, the PV panel voltage and the generated power. The power and voltage characteristics of a shaded PV panel, considering the worst-case scenario, are half of the nominal output voltage and a third of the output power [2]. For the sake of simplicity, it is considered that all the PV panels are exactly equaled. Two different voltage and power characteristics are therefore defined, one for the non-shaded PV panels (29.3 V and 225 W) and the other one for the shaded ones (15 V and 67.5 W).

In a DMPPT architecture, the expression (38) is fulfilled by all the MIC connected to the same string.

$$i_{string} = \frac{p_{string}}{v_{string}} \tag{38}$$

Being p_{string} and v_{string} the power generated in the string and the voltage of the string respectively.

As aforementioned, the central inverter fixes the string voltage. Considering the ideal case, where the efficiency of the MIC is 100 %, the power generated by the PV panel is the same as the power delivered from the converter to the string; i.e. $P_{in} = P_{out}$. Therefore, assuming this statement, the output voltage of each converter can be obtained through the whole power generated in the string and the power delivered by the PV panel to the string, see (39).

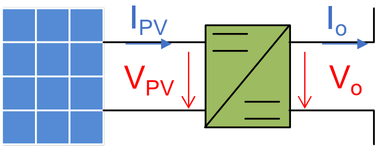

Figure 19. Detail of the connection between the PV panel and the MIC

$$V_o = \frac{V_{PV} \cdot I_{PV}}{I_o} = \frac{V_{PV} \cdot I_{PV}}{p_{string}} \cdot v_{string} = \frac{p_{PV}}{p_{string}} \cdot v_{string} \qquad (39)$$

For Scenario E1, applying the power reduction in the shaded PV panels, the delivered power per string, p_{string}, can be obtained. Finally, with (39), the output voltage of the converters under both scenarios are obtained.

The case-of-study specifications are summarised in Table VI.

Table VI. Case of study parameters summary

Converter	Parameter	Scenario E0	Scenario E1
Non-shaded PV panel	Power (W)	225	225
	V_i (V)	29.3	29.3
	V_o (V)	33.3	40.404
	I_{string} (A)	6.75	5.569
Shaded PV panel	Power (W)	N/A	67.5
	V_i (V)	N/A	15
	V_o (V)	N/A	12.121
	I_{string} (A)	N/A	5.569

It is noteworthy that, in strings with shaded PV panels, the converters attached to the non-shaded PV panels have to step-up their output voltages whereas the ones attached to the shaded PV panels have to step-down its output voltage. This performance can only be achieved with a voltage step-up and step-down converter.

3.1.2 Design procedure: selection of the AFF converter components

In this section, a step-by-step design procedure is applied to the aforementioned case of study.

- Step 1: Stablish the highest voltage step-up for the application of interest. The AFF converter does not present any voltage step-down limitation.
- Step 2: The AFF converter with both the output inductor and the autotransformer operating on CCM (OM1) should fulfil the conditions (4) and (5). In both expressions, there are three independent variables: n, n_d and d. For solving the system equation, one more condition is added (40)

$$n = n_d \qquad (40)$$

The condition (40) is established to make easier the Autotransformer design and to reduce the leakage inductance.

- Step 3: With the three expressions (4), (5) and (40), there is a minimum n and n_d value per maximum duty cycle and voltage step-up ratio. The solutions of the system of equations are depicted in Figure 20.

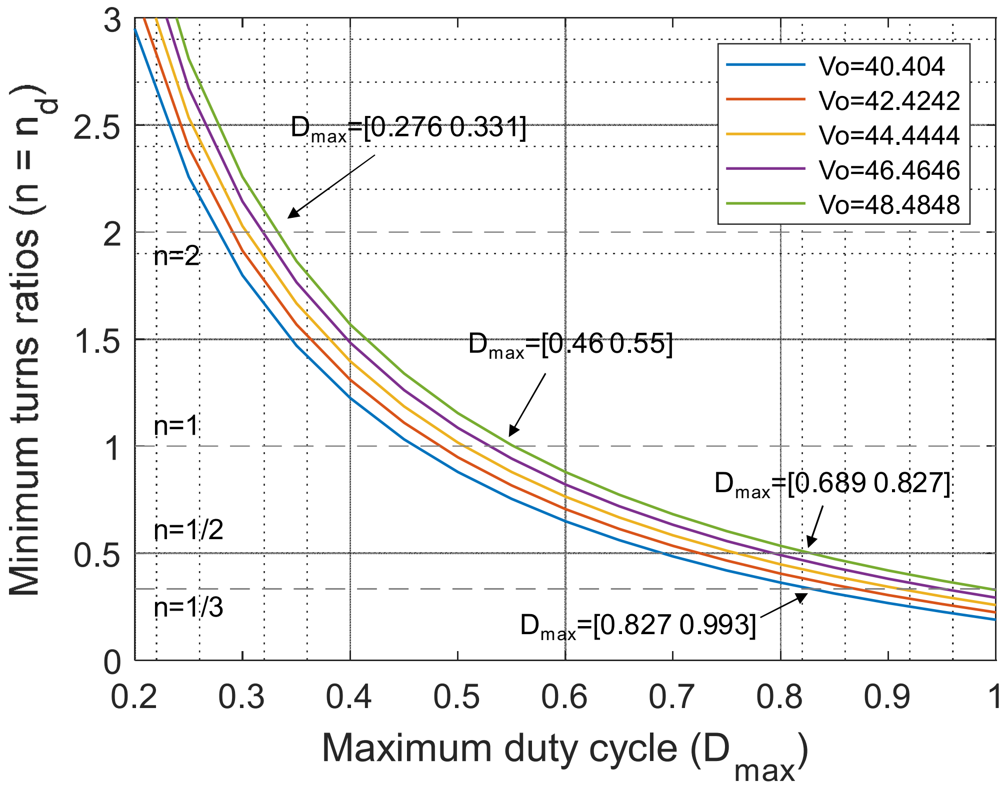

Figure 20. Possible turns ratios values for the AFF converter autotransformer, for different output voltages and maximum duty cycles.

Although the maximum output voltage of the application is $V_0 = 40.404\,V$, several curves are depicted in order to obtain a maximum duty cycle range for each turns ratio value. Four turns ratios values are highlighted.

As it can be seen, higher turns ratio values yield in lower maximum duty cycle. Therefore, to improve the duty cycle range, low turns ratio values are desired. On the other hand, low turns ratio values increase the voltage stresses that the MOSFET, the D_1 diode and the D_2 diode withstand. As a tradeoff, $n = n_d = 0.5$ is selected as the optimum turns ratio values for the case of study described in Section 3.1.1.

Once these three steps are carried out, the specifications for the AFF converter are obtained, see Table VII.

Table VII. Specifications for the converter design

Parameter	Specification	Parameter	Specification
V_i (V)	[15-29.3]	D_{max}	0.75
V_o (V)	[12-40.404] ±10%	P_{omax} (W)	225
D_{min}	0	P_{omin} (W)	60

- Step 4: Obtain the electrical stresses in each element of the AFF converter. Section 2.2 details the voltage and current expressions for each component, considering a switching frequency $f_s = 50\ kHz$. The maximum values are used for selecting the appropriate devices for the AFF converter prototype. In Table VIII are summarized the main parameters of the selected components.

Table VIII. Maximum electrical stresses in the AFF components.

Component	Voltages (V)	Currents (A)	Other characteristics	Selected Part-reference
C_i	$V_{Ci}{}^{(*)} = 35.16$	$I_{Ci\_rms} = 6.87$	$C_{i\_min} = 178.8\ \mu F$	C_50SVPF68M *(x4)*
C_o	$V_{Co}{}^{(*)} = 48.48$	$I_{Co\_rms} = 1.06$	$C_{o\_min} = 26.2\ \mu F$	C_EEHZA1J560P *(x2)*
C_{aux}	$V_{Caux}{}^{(*)} = 38.95$	$I_{Caux\_rms} = 0.93$	$C_{o\_min} = 18\ \mu F$	C_EEHZA1H101P
S	$V_{S\_OFF} = 94.36$	$I_{S\_peak} = 17.15$ $I_{S\_rms} = 10.31$	$R_{DS\_on} = 9.5\ m\Omega$ $Q_g = 45\ nC$	FDMS86255ET150
D_1	$V_{D1} = 129.82$	$I_{D1} = 3.84$ $I_{D1\_peak} = 8.58$	$V_f \approx 1.2\ V$	C3D08065E
D_2	$V_{D2} = 24.62$	$I_{D2} = 2.91$ $I_{D2\_peak} = 8.58$	$V_f \approx 0.09\ V$	SPV1002T40
D_d	$V_{Dd\_ON} = 47.18$	$I_{Dd} = 2.91$ $I_{Dd\_peak} = 8.55$	$V_f \approx 0.33\ V$	V40D100C-M3/I
L	$V_{L\_ON} = 10.62$ $V_{L\_OFF} = 14.01$	$\Delta I_L = 3.66$ $I_L = 6.75$ $I_{L\_rms} = 6.832$	$L = 33\ \mu H$ $DCR = 13.2\ m\Omega$	74435583300
Autotransformer (L_m)	$V_{Lm\_ON} = 29.3$ $V_{Lm\_OFF1} = 65.06$	$I_{Lm} = 2.184$ $I_{Lm\_peak} = 3.375$ $I_{Lm\_rms} = 3.415$	$n = 0.5$ $n_d = 0.5$ $L_m = 185\ \mu H$ $L_{leakage} = 190\ nH$	Non-standard part $RM12 - 3C90\ core.$

(*) A 20% margin is considered in the input and output voltages, see Table VII.

As it can be seen in the characteristics of the selected AFF converter components, the D_2 diode presents a very low forward voltage drop V_f. This property is desired for reducing the power losses. The selection of this device is possible thanks to low voltage that withstand, due to the C_{aux} placement.

Besides the components summarised in Table VIII, three snubber nets, a driver and a current sensor have been designed and implemented in the AFF prototype, see Figure 21.

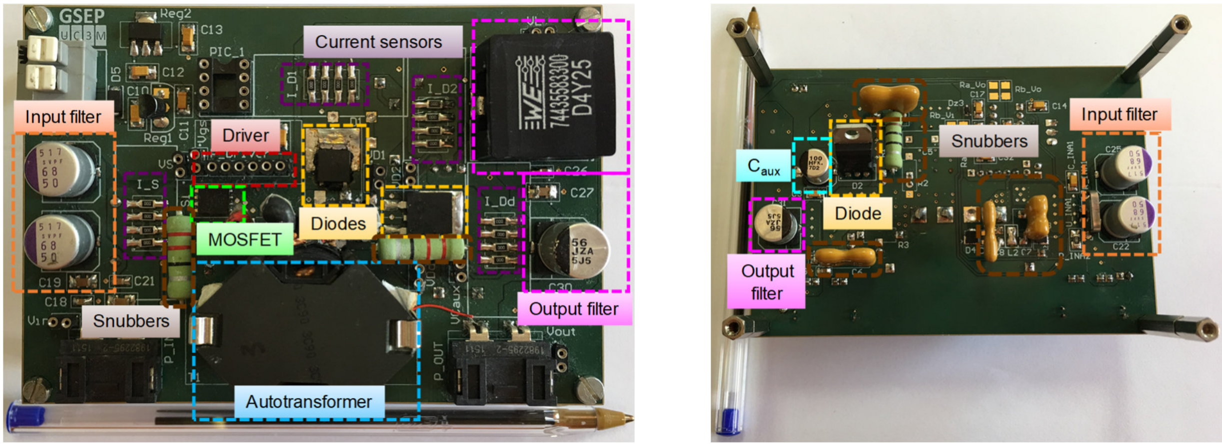

a) b)

Figure 21. AFF prototype. a) TOP view; b) BOTTOM view

Typical R-C dissipative snubber net is added in parallel to the D_2 and D_d diodes. For reducing the voltage spike on the MOSFET, a backward-regenerative and a dissipative snubber nets are used. Both typical electrical schemes are shown in Figure 22.

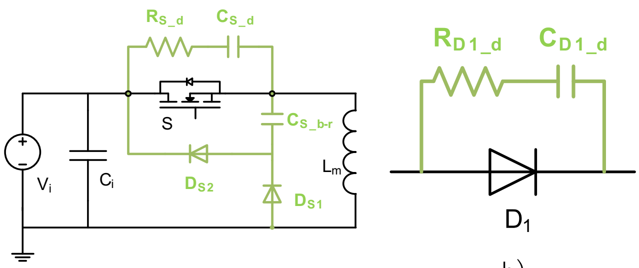

a) b)

Figure 22. Snubber nets electrical schemes. a) MOSFET snubber nets; b) D_1 diode snubber net

The design of the snubber networks is based in [37]. The components that form the backward-regenerative type snubber are the D_{S1}, D_{S2} and C_{S_b-r}, whereas the dissipative snubber type components are denoted with the suffix d. The selected capacitors and resistors employed as snubber nets are summarized in Table IX.

Table IX. Parameters of the snubber nets added to the AFF prototype

Component	Value	Component	Value
R_{S_d}	22Ω	R_{D2_d}	100Ω
C_{S_d}	2.2nF	C_{D2_d}	680pF
C_{S_b-r}	1nF	R_{Dd_d}	22Ω
		C_{Dd_d}	680pF

Due to the MOSFET position, an isolated driver is required. For this purpose, a pulse transformer is used. The scheme of the driver is detailed in Figure 23.

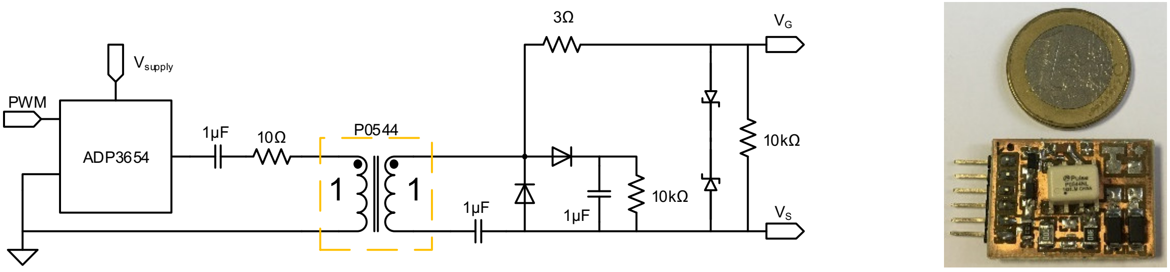

a) b)

Figure 23. Driver electrical scheme in a); Driver picture of the prototype in b)

The current sensor is based in a current-sensing transformer, see Figure 24.

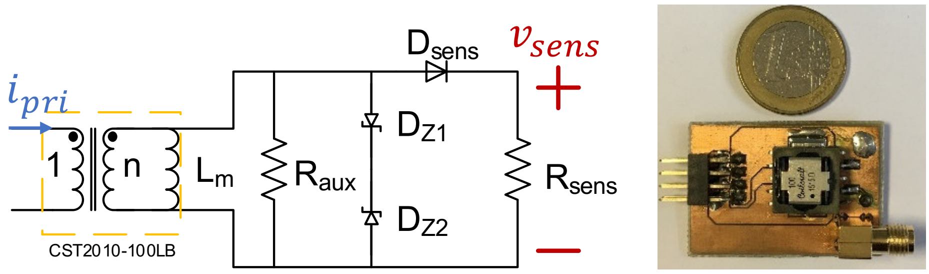

a) b)

Figure 24. Current sensor electrical scheme in a); current sensor picture of the prototype in b)

Where the turn ratio of the current-sensing transformer is $n = 100$ and the sensing resistance value is $R_{sens} = 50\ \Omega$. Due to these two parameters, the current through the transformer primary side is, in amperes, twice the volts sensed between the sensing resistance terminals (41).

$$i_{pri} = 2 \cdot v_{sens} \tag{41}$$

3.2 Time domain measurements

In this section, the most relevant time domain waveforms of the Autotransformer Forward-Flyback converter are shown. The test conditions are the same as described in the Scenario E0, see Table VI. The current waveforms are depicted in green colour whereas the voltage ones are depicted in yellow colour.

Figure 25 shows the S MOSFET current and voltage waveforms.

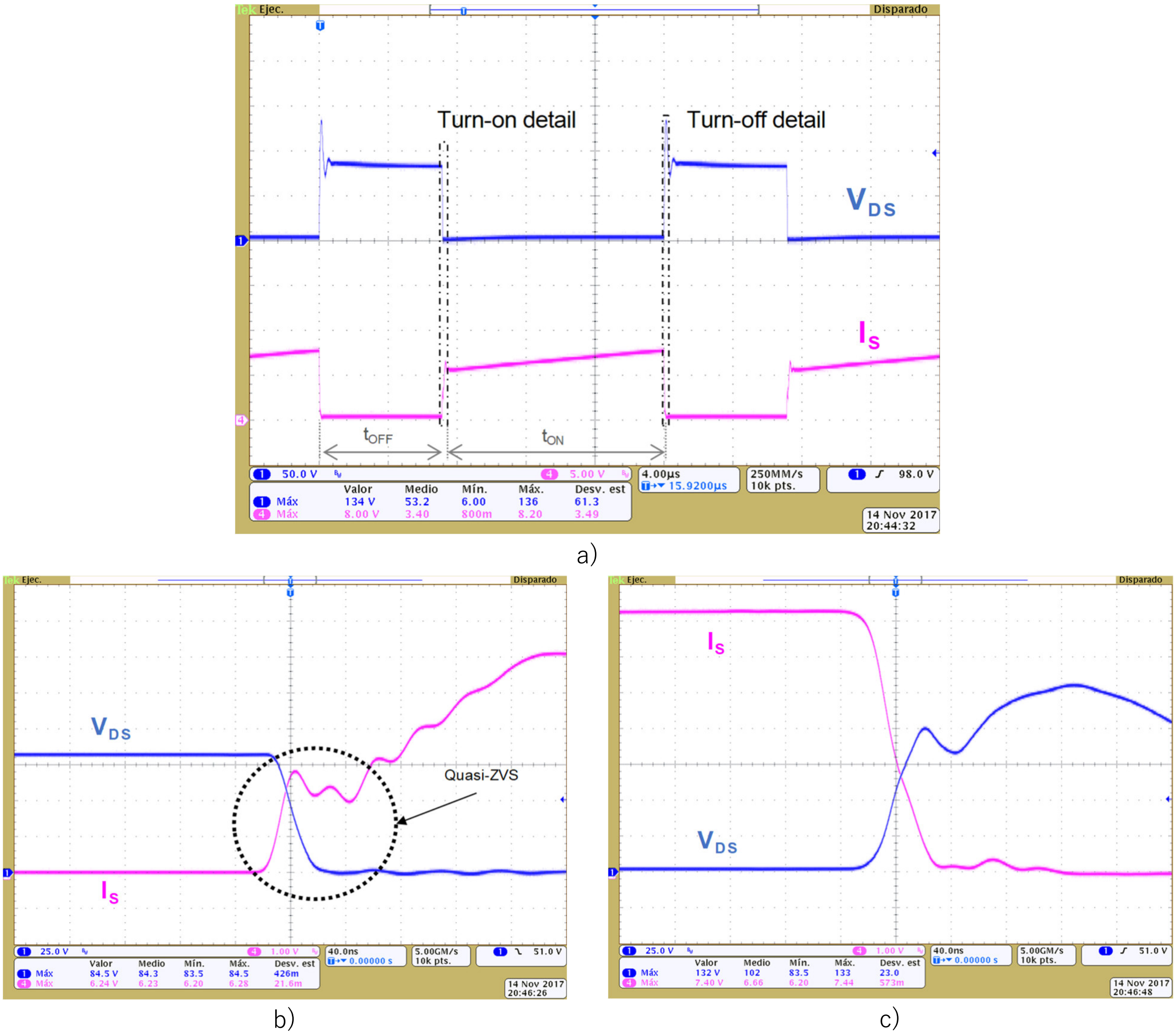

Figure 25. MOSFET waveforms. V_{DS} in yellow colour and I_S in green colour. a) complete switching period; b) turn-on detail; c) turn-off detail

In Figure 25a) can be seen that the steady state values are the expected ones for the MOSFET waveforms, see Figure 10. Regarding the transitions, it is noteworthy that the MOSFET presents Quasi-ZVS during the turn-on transition, due to the amount of current rising during the voltage falling edge is around a 40 % of the maximum rising current. In the turn-off transition, it presents hard-switching.

In Figure 26, the D_1 diode waveforms are depicted.

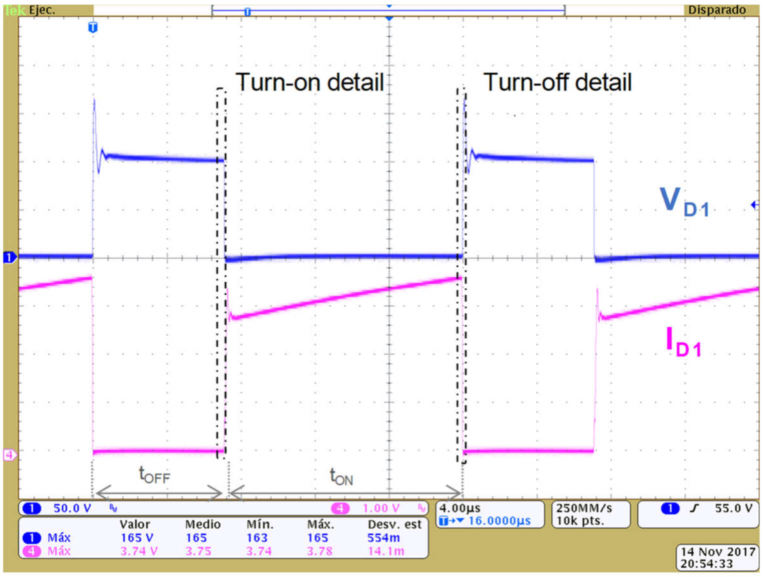

a)

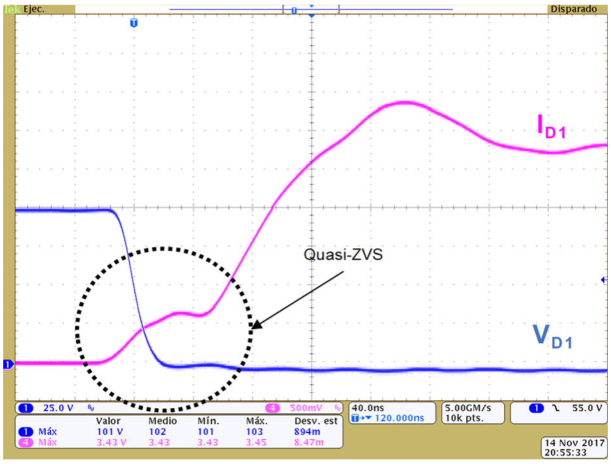

b)

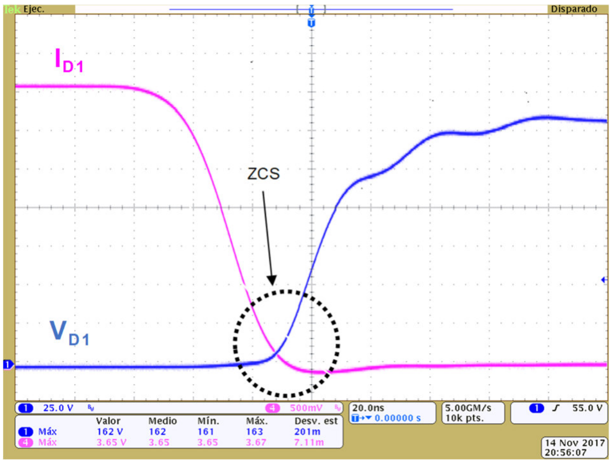

c)

Figure 26. D_1 diode waveforms. V_{D1} in yellow colour and I_{D1} in green colour. a) complete switching period; b) turn-on detail; c) turn-off detail

During the t_{OFF} interval, the D_1 diode receives a similar voltage and current waveforms compare to MOSFET, as can be appreciated in Figure 25a) and Figure 26a).

In Figure 26b) can be seen that D_1 diode has Quasi-ZVS when turn-on. In this case, the maximum current value achieved during the voltage falling edge is around 10 % of the maximum rising current. On the other hand, during the turn-off, see Figure 26c), the AFF converter has Zero Current Switching (ZCS). Therefore, very low switching losses are expected in the D_1 diode. For the D_1 diode, the time base is zoomed from 40 ns to 20 ns to better shown the ZCS transition.

The D_2 diode waveforms are depicted in Figure 27.

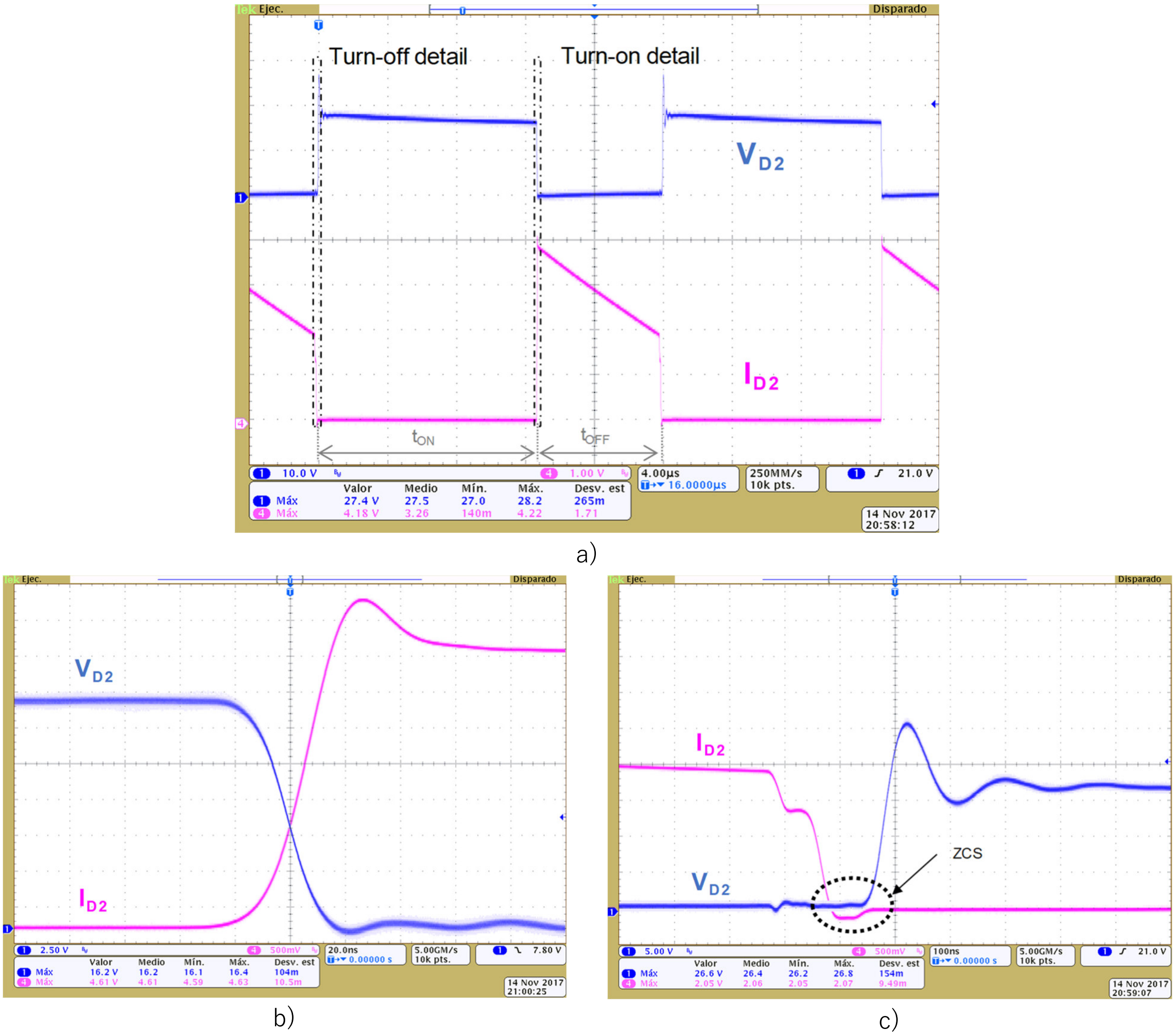

Figure 27. D_2 diode waveforms. V_{D2} in yellow colour and I_{D2} in green colour. a) complete switching period; b) turn-on detail; c) turn-off detail

Low D_2 switching losses are expected thanks to the ZCS at the turn-off transition, see Figure 27c). Also, thanks to the very low forward voltage drop in this diode, low DC losses are also expected. In the turn-on transition, it presents hard-switching, Figure 27b).

The last oscilloscope measurements refer to the D_d diode, see Figure 28.

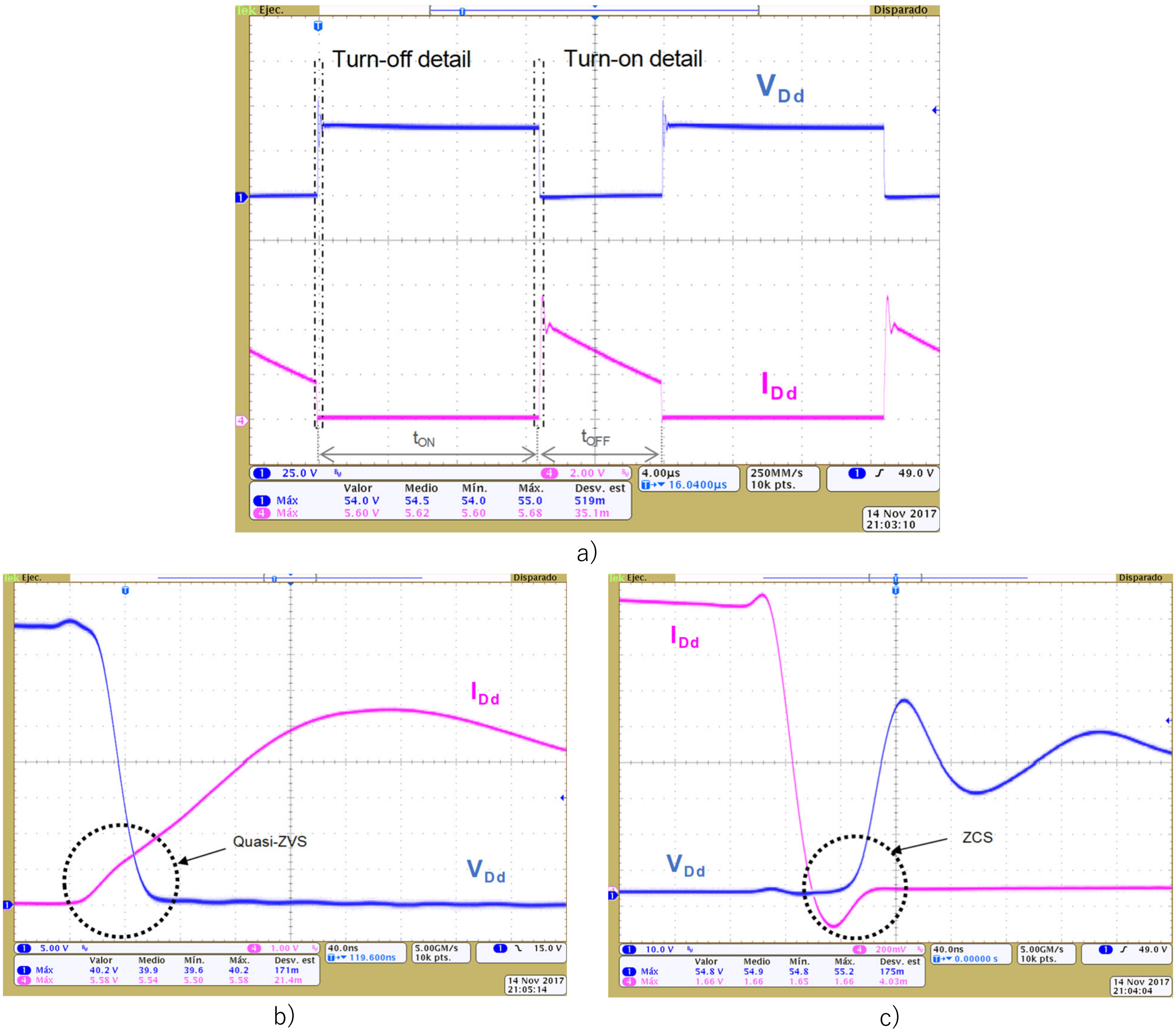

Figure 28. D_d diode waveforms. V_{Dd} in yellow colour and I_{Dd} in green colour. a) complete switching period; b) turn-on detail; c) turn-off detail

Due to the Flyback-net of the AFF converter, the autotransformer reset is similar to the Flyback converter one. It means that the magnetising current flows through the D_d, D_2 diodes as well as through the output filter. A ZCS and a Quasi-ZVS performance are also present in this diode during the turn-on and turn-off intervals respectively. Therefore, low switching losses are expected in the D_d diode.

Comparing the current and voltage waveforms shown in Figure 26 - Figure 28, with the theoretical ones, see Figure 10 - Figure 13 respectively, the steady-state theoretical analysis is verified, as well as the proper operation of the AFF converter.

3.2.1 Efficiency analysis

The efficiency is measured using the Yokogawa WT3000. The efficiency graphs shown in Figure 29 are obtained for the corresponding input and output voltages detailed in Table VI.

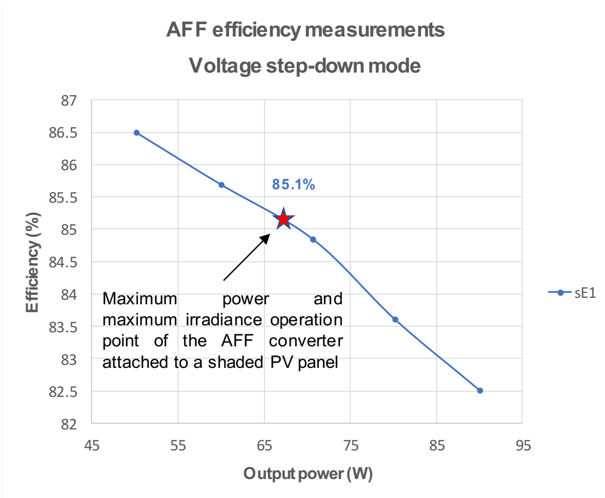

a)

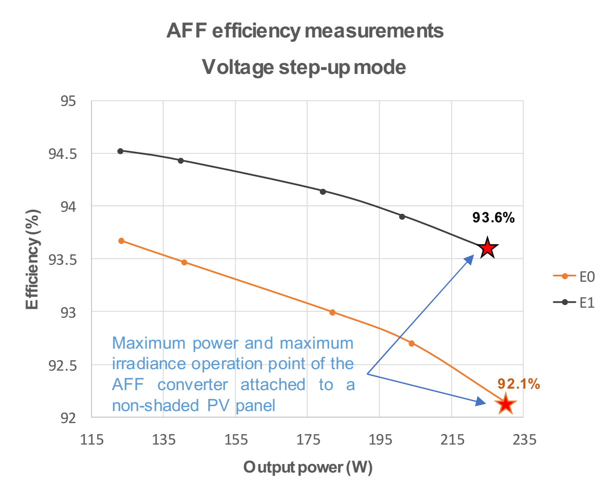

b)

Figure 29. AFF efficiency measurements. A) Efficiencies for the shaded PV panel converter; b) Efficiencies for the non-shaded PV panel converter

The measurement shown in Figure 29.a) emulates the performance of the AFF converter while attached to a shaded PV panel. Therefore, the input and output voltages are fixed to 15 V and 12.12 V respectively. The performance while attached to a non-shaded PV panel is shown in Figure 29.b). The voltage ranges employed in Scenario E0 and E1 are detailed in Table VI.

As it can be seen in Figure 29, the higher the output voltage, the higher the efficiency of the AFF converter. Also, the higher the output power, the lower the efficiency. Both conclusions are related to the conduction losses, which are more relevant than the switching losses. The AFF converter efficiency, when it is connected to a PV panel in shaded conditions, Figure 29.a), is the lowest. The maximum measured efficiency is 94.5 %, and it is quite constant from half load to full load, varying around 1 %.

The Buck-Boost converter, the Cúk converter with a coupled inductor and the Non-Inverting Buck-Boost converter have been considered as the main MIC competitors, due to all of them are non-isolated voltage step-up and step-down converters, commonly applied to photovoltaic systems. Table X includes a comparison between them and the AFF converter.

Table X. Comparison between the AFF converter with the Buck-Boost converter, the Cúk converter with a coupled inductor and the Non-Inverting Buck-Boost converter

Parameters	AFF	Buck-Boost [30]	Cúk with coupled inductor [30]	Non-Inverting Buck-Boost [27]
Magnetic components	2	1	1	1
Active switches	1	1	1	4
Drivers	1	1	1	4
Passive switches	3	1	1	0
Dynamic performances	No-RHP zero	RHP zero	RHP zero	RHP zero
Efficiency (%)	94.5	87.2	93.1	98.5

As it can be deduced from the comparison shown in Table X, the efficiency of the AFF converter is comparable with the efficiencies obtained with other topologies for this application [30]. Although the Cúk converter's component count is lower than for the AFF converter, their diode, main capacitor and active switch withstand high electrical stresses. Moreover, its dynamic response is slower due to the RHP zero in the small signal transfer functions. Recent works have reported higher efficiencies with the Non-Inverting Buck-Boost converter, see [14] and [27], but including four controlled switches and drivers. In comparison to them, the AFF semiconductor count is limited to three diodes and one power MOSFET, and therefore only a driver, resulting in potential cost reductions. This fact simplifies the converter and improves the reliability of the overall system. Besides, the size of the output filter capacitors in the AFF converter is lower due to its output filter inductor. It is notable that all the competitors suffer from RHP zero in their small signal transfer functions, limiting their dynamic performance.

4. CONCLUSIONS

The theoretical analysis of the Autotransformer Forward-Flyback (AFF) converter is carried out in this paper, including the steady-state and time domain analysis as well as the small-signal analysis with both the output inductor and the autotransformer operating in continuous conduction mode.

Regarding the steady-state analysis, the main points analysed in the paper are the principle of operation of the AFF converter, the voltage and current expressions of each component and the output-input voltage transfer function.

The frequency domain analysis includes the obtaining of the main small signal transfer functions, meaning the output voltage – duty cycle ($G_{vd}(s)$), the audiosusceptibility ($G_{vv}(s)$) and the output impedance ($Z_o(s)$) small signal transfer functions. The analytical results are validated through simulation. Two poles-pairs appear in all the transfer functions, corresponding each poles-pair to the Forward-net and Flyback-net of the AFF converter.

A step-by-step procedure describes how to design the AFF converter for any field of application. A case of study with two different shading conditions is described and used for the design of the 225 W prototype.

The measured results in a 225 W prototype verify the theoretical analysis. It has been highlighted that some MOSFET and diodes switching present ZCS and, in particular, the D_1 diode, which has high influence in the converter efficiency, present both ZCS and quasi-ZVS. The effect of some parasitic inductances, not considered in the theoretical analysis, are shown and explained with the measured waveforms.

The efficiency of the AFF converter is described through a set of measurements for the input-and-output voltage conditions of each Scenario. The highest measured efficiency is 94.5 %.

Summarizing, the main advantages of the AFF converter are its step-up and step-down voltage transfer function; the ZCS and quasi-ZVS characteristics in the diodes, yielding in efficiencies up to 94.5 %; the use of an autotransformer, with better performances than a typical Forward transformer; and the use of a single controlled switch. This last advantage can result in a potential reduction of cost and increase of reliability. On the other hand, the main drawbacks of the introduced converter are the high voltage stresses in the D_1 diode and MOSFET. Hence, those devices able to withstand higher voltages but with worse performances are selected. Also, snubber networks must be added to mitigate these voltage spikes due to leakage inductance, yielding in an efficiency reduction. Although it is not a requirement for the field of application, the output of the converter is not isolated from the input, due to the use of an autotransformer. Finally, the AFF converter does not present RHP zero in their small signal transfer functions, and therefore a good dynamic performance is achieved.

Acknowledgements

This work has been supported by the Ministry of Economy and Competitiveness and FEDER funds through the research project "Storage and Energy Management for Hybrid Electric Vehicles based on Fuel Cell, Battery and Supercapacitors" - ELECTRICAR-AG- (DPI2014-53685-C2-1-R)

References

[1] Arnulf Jäger-Waldaul, “Snapshot of photovoltaics - February 2018”, EPJ Photovolt. 9, 6 (2018). DOI: 10.1051/epjpv/2018004

[2] Orduz, R.; "Contrubución a los sistemas de control de potencia micro-distribuida en edificios fotovoltaicos". PhD Thesis, 2009, Universidad Politécnica de Madrid.

[3] E. Forniés, et al, "The influence of mismatch of solar cells on relative power loss of photovoltaic modules" Original Research Article. Solar Energy, Volume 97, November 2013, pp. 39-47

[4] E. Díaz-Dorado, J. Cidrás, and C. Carrillo, “Discrete I-V model for partially shaded PV-arrays,” Sol. Energy, 2014.

[5] D. Picault, B. Raison, S. Bacha, J. de la Casa, and J. Aguilera, “Forecasting photovoltaic array power production subject to mismatch losses,” Sol. Energy, 2010.

[6] D. G. Lorente, S. Pedrazzi, G. Zini, A. Dalla Rosa, and P. Tartarini, “Mismatch losses in PV power plants,” Sol. Energy, vol. 100, 2014.

[7] A. Rico, et al, "Power Injection Control System and Experimental Model based on Manufacturer Characteristic Curves for a Photovoltaic Generation System", in 2007 Compatibility in Power Electronics, CPE'07, Digital object Identifier: 10.1109/CPE.2007.4296501, pp. 1-7

[8] Femia, N.; Lisi, G.; Petrone, G.; Spagnuolo, G.; Vitelli, M. "Distributed Maximum Power Point Tracking of Photovoltaic Arrays: Novel Approach and System Analysis" Industrial Electronics, IEEE Transactions on Volume: 55 , Issue: 7 DOI: 10.1109/TIE.2008.924035 Publication Year: 2008, Page(s): 2610 - 2621T. Esram, P.L. Chaoman, "Comparison of Photovoltaic Array Maximum Power Point Tracking Techniques", IEEE Transactions on Energy Conversion 2007, Volume: 22, Issue: 2. Digital Objet Identifier:

[9] G. R. Walker and P. C. Sernia, “Cascaded DC/DC Converter Connection of Photovoltaic Modules,” IEEE Trans. Power Electron., vol. 19, no. 4, pp. 1130–1139, 2004.10.1109/TEC.2006.874230, pp. 439-449.

[10] A. Elasser, et al, "A Comparative Study of Central and Distributed MPPT Architectures for Megawatt Utility and Large Scale Commercial Photovoltaic Plants", in the 36th Annual Conference on IEEE Industrial Electronics Society (IECON) 2010, Digital Objet Identifier: 10.1109/IECON.2010.5675108.347797, pp. 2753-2758

[11] N. Femia, G. Lisi, G. Petrone, G. Spagnuolo, and M. Vitelli, “Distributed Maximum Power Point Tracking of Photovoltaic Arrays : Novel Approach and System Analysis,” IEEE Trans. Ind. Electron., vol. 55, no. 7, pp. 2610–2621, 2008.

[12] S. Poshtkouhi, V. Palaniappan, O. Trescases, "A General Approach for Quantifying the Benefit of Distributed Power Electronics for Fine Grained MPPT in Photovoltaic Applications Using 3-D Modeling", IEEE Transactions in Power Electronics 2012. Volume:27, Issue:11, Digital Object Identifier: 10.1109/TPEL.2011.2173353, pp. 4656-4666

[13] Bratcu, et al, "Power Optimization Strategy for Cascaded DC-DC Converter Architectures of Photovoltaic Modules", in IEEE International Conference on Industrial Technology, 2009. ICIT 2009. Digital Object Identifier:10.1109/ICIT.2009.4939559, pp.1-8

[14] L. Linares, et al "Improved Energy Capture in Series String Photovoltaics via Smart Distributed Power Electronics", in Twenty-Fourth Annual IEEE Applied Power Electronics Conference and Exposition 2009, APEC'09. Digital Objet Identifier: 10.1109/APEC.2009.4802770, pp. 904-910

[15] R.M. Button, "An advanced photovoltaic array regulator module", in the Proceedings of the 31st Intersociety Energy Conversion Engineering Conference, 1996, IECEC'96. Volume:1, Digital Objet Identifier: 10.1109/IECEC.1996.552937, pp. 519-524

[16] H. Kim, et al, "A highly efficient PV system using a series connection of DC-DC converter output with a photovoltaic panel", Original Research Article Renewable Energy, Volume 34, Issue 11, November 2009, Pages 2432-2436

[17] D. L. Moral et al., “Static and Dynamic Analysis of a 300W Series Connection Flyback Converter Applied to Photovoltaic Panels, ” pp. 350–357, 2015.

[18] P.J. Villegas, et al, "Average Current Mode Control of Series-Switching Post-Regulators Used in Power Factor Correctors", in IEEE Transactions on Power Electronics 2000. Volume:15, Issue:5. Digital Object Identifier. 0.1109/63.867669, pp. 813-819

[19] E. Bataller-Planes, et al, "Power Balance of a Hybrid Power Source in a Power Plant for a Small Propulsion Aircraft" in IEEE Transactions on Power Electronics 2009. Volume:24, Issue:12. Digital Object Identifier. 10.1109/TPEL.2009.20229439, pp. 2856-2866

[20] L. Jong Pil, et al, "A Novel Topology for Photovoltaic Series Connected DC/DC Converter with High Efficiency Under Wide Load Range", in IEEE Power Electronics Specialists Conference 2007. Digital Object Identifier. 10.1109/PESC.2007.4341979, pp. 152-155

[21] K. Heeje, et al,"A high efficiency photovoltaic module integrated converter with the asymmetrical half-bridge flyback converter ", Original Research Article. Solar Energy, Volume 84, Issue 8, August 2010, Pages 1376-1381

[22] H. Dehbonei, S.R. Lee, S.H. Ko, "Direct Energy Transfer for High Efficiency Photovoltaic Energy Systems Part I: Concepts and Hypothesis" in IEEE Transactions on Aerospace and Electronic Systems 2009; Volume:45, Issue:1. Digital Object Identifier: 10.1109/TAES.2009.4805261, pp. 31-45

[23] H. Dehbonei, S.R. Lee, S.H. Ko, "Direct Energy Transfer for High Efficiency Photovoltaic Energy Systems Part II: Experimental Evaluations" in IEEE Transactions on Aerospace and Electronic Systems 2009; Volume:45, Issue:1. Digital Object Identifier: 10.1109/TAES.2009.4805262, pp. 46-57

[24] T. Labella et al., "A Bidirectional-Switch-Based Wide-Input Range High-Efficiency Isolated Resonant Converter for Photovoltaic Applications," vol. 29, no. 7, pp. 3473–3484, 2014.

[25] H. Fathabadi, "Novel high efficiency DC / DC boost converter for using in photovoltaic systems," vol. 125, pp. 22–31, 2016.

[26] H. Luo, H. Wen, X. Li, L. Jiang, and Y. Hu, "Synchronous buck converter based low-cost and high-efficiency sub-module DMPPT PV system under partial shading conditions," vol. 126, pp. 473–487, 2016.

[27] M. Kasper, D. Bortis, and J. W. Kolar, "Classification and comparative evaluation of PV panel-integrated DC-DC converter concepts," IEEE Trans. Power Electron., vol. 29, no. 5, pp. 2511–2526, 2014.

[28] G. Dileep and S. N. Singh, "Selection of non-isolated DC-DC converters for solar photovoltaic system," Renew. Sustain. Energy Rev., vol. 76, no. August 2016, pp. 1230–1247, 2017.

[29] J. M. Enrique, E. Durán, M. Sidrach-de-Cardona, and J. M. Andújar, "Theoretical assessment of the maximum power point tracking efficiency of photovoltaic facilities with different converter topologies," Sol. Energy, vol. 81, no. 1, pp. 31–38, 2007.

[30] M.H. Taghvaee, et al, "A current and future study on non-isolated DC–DC converters for photovoltaic applications", Review Article Renewable and Sustainable Energy Reviews, Volume 17, January 2013, Pages: 216-227

[31] A. Chakraborty, A. Khaligh, and A. Emadi, "Combination of buck and boost modes to minimize transients in the output of a positive buck-boost converter," IECON Proc. (Industrial Electron. Conf., pp. 2372–2377, 2006.

[32] D. López del Moral; A. Barrado; M. Sanz; A. Lázaro; P. Zumel "A new DC-DC buck-boost modified series forward converter for photovoltaic applications" 2014 IEEE Energy Conversion Congress and Exposition (ECCE) Year: 2014 Pages: 1887 – 1894

[33] D. López del Moral, A. Barrado, M. Sanz, A. Lazaro, C. Fernandez, and P. Zumel, "High efficiency DC-DC autotransformer forward-flyback converter for DMPPT architectures in solar plants," *Proc. - 2015 9th Int. Conf. Compat. Power Electron. CPE 2015*, pp. 431–436, 2015.

[34] Erickson, R.; "Fundamentals of Power Electronics". Editorial Kluwer Academic Publisher, 2000. Segunda edición. ISBN: 0-7923-7270-0. Páginas: 883

[35] Power Electronics, "Freesun LVT Catalog" http://www.power-electronics.com/184.html?Freesun+LVT+Descarga. Last view on 15 June 2014.

[36] Siliken, "SLK60P6L PV panel" http://www.siliken.com/ www.siliken.com/cargas/MultiCrystallineDataSheet_EN.pdf. Last view on 15 June 2014.

[37] Ben-Gurion University of the Negev; "DESIGN OF SNUBBERS FOR POWER CIRCUITS.pdf". Downloaded in: https://wwwee.ee.bgu.ac.il/~pel/links/DESIGN_OF_SNUBBERS_FOR_POWER_CIRCUITS.pdf. Last view on 17 May 17, 2018